Applied Catalysis B: Environmental 211 (2017) 114–125

Contents lists available at ScienceDirect

Applied Catalysis B: Environmental

journal homepage: www.elsevier.com/locate/apcatb

Photocatalytic activity of mont-La (6%)-$Cu_{0.6}Cd_{0.4}S$ catalyst for phenol degradation under near UV visible light irradiation

H. Boukhatem[a,b,d], H. Khalaf[b], L. Djouadi[b], F.V. Gonzalez[c], R.M. Navarro[c], J.A. Santaballa[d], M. Canle[d,*]

[a] Département des Sciences de la Matière, Faculté des Sciences et de la Technologie, Université Djilali Bounaama de Khemis-Miliana, Route de Theniet El Had, 44001 Khemis-Miliana, Algeria
[b] Laboratoire de Génie Chimique, Département de Génie des procédés, Faculté de Technologie, Université Saad Dahleb-Blida 1, BP270-09000-Blida, Algeria
[c] Instituto de Catálisis y Petroleoquímica (CSIC), C/Marie Curie 2, Cantoblanco, E-28049 Madrid, Spain
[d] Chemical Reactivity and Photoreactivity Group, Dept. of Chemistry, Faculty of Sciences & CICA, University of A Coruña, E-15071 A Coruña, Spain

ARTICLE INFO

Article history:
Received 26 December 2016
Received in revised form 28 March 2017
Accepted 29 March 2017
Available online 9 April 2017

Keywords:
Photocatalysis
Semiconductor sulfides
Phenol
UV–vis
Pollution abatement
Persistent organic pollutants
Modified clays
Montmorillonite
Nanocomposites

ABSTRACT

A mont-La (6%)-$Cu_{0.6}Cd_{0.4}S$ nanocomposite was prepared by a simple cation exchange and impregnation method and its application for the phenol removal from wastewater was studied. The photocatalyst was characterized by X-ray diffraction (XRD), Fourier transform infrared spectroscopy (FTIR), scanning electron microscopy (SEM), energy dispersive X-ray spectroscopy (XEDS) and UV–vis diffuse reflectance spectroscopy (UV–vis DRS). Phenol in aqueous solution was used as a model compound for evaluation of near UV–vis (filter cut-off for $\lambda \geq 366$ nm) photocatalytic activity. We have studied the following parameters: load of photocatalyst, load of phenol, pH, $[O_2]$, and irradiation wavelength. Within 240 min, heterogeneous suspensions of 1 $g \cdot L^{-1}$ of mont-La (6%)-$Cu_{0.6}Cd_{0.4}S$ nanocomposite allowed removal of ca. 86% of 20 $mg \cdot L^{-1}$ solution of phenol at pH = 5.44, with dissolved oxygen from air, with 77.8% TOC removal. The kinetics of photocatalytic transformation followed the Langmuir–Hinshelwood kinetic model. Pseudo-first-order kinetics adequately fitted the experimental data and the obtained rate constants are reported. With the mont-La (6%)-$Cu_{0.6}Cd_{0.4}S$ catalyst 84% removal of phenol degradation efficiency was achieved after five consecutive photocatalytic cycles. Twelve main photoproducts were observed from phenol photodegradation, using HPLC–MS. The used photocatalyst is promising for green chemistry use in abatement of persistent organic pollutants.

© 2017 Elsevier B.V. All rights reserved.

1. Introduction

The release of toxic and persistent organic pollutants (POPs) into the aquatic environment is a matter of growing concern, and addressing this issue for remediation is considered to be an urgent environmental need [1]. Many persistent organic pollutants, which are highly toxic and hazardous to human health and ecosystems, are present in industrial wastewaters from chemical factories [2], and are responsible for contamination of ground and surface water [1]. The biodegradability of these compounds is usually very low, leading to their accumulation in the environment [2].

Among POPs, phenol and its derivatives are generally considered as some of the most relevant organic pollutants discharged into the environment, considered by the US EPA as some of the most pollutant compounds, causing considerable damage to human health and to the ecosystems [3] and recognized as carcinogenic compound [4]. Phenols are harmful to living organisms even at low concentrations [5]. They are easily absorbed through the skin and mucous membranes, and toxic to different organs and tissues: lungs, liver, kidneys, and genitourinary system [6]. They are released from herbicides, pesticides, textiles, dyes, paints, oil refining, coal conversion, plastics, pharmaceutical, chemical, agrochemical, and petrochemical industries, etc. [3,7–10]. Phenol, with rather high solubility [11], causes unpleasant taste and odor of drinking water [5,12].

For all the above mentioned reasons, phenols have been listed as priority pollutants for degradation by many governmental environmental agencies [4]. It has become a challenge to achieve an effective removal of this POP from wastewater, to minimize risks. Consequently, considerable efforts have been devoted to develop suitable treatment methods that can easily get rid of these highly recalcitrant POPs [12].

* Corresponding author.
E-mail address: mcanle@udc.es (M. Canle).

http://dx.doi.org/10.1016/j.apcatb.2017.03.074
0926-3373/© 2017 Elsevier B.V. All rights reserved.

Phenols can be treated by different conventional processes such as adsorption, electrochemical oxidation, and biological treatment to meet its safety discharge level which is in the range of 0.1–1.0 mg·L^{-1} [13]. However, these processes generate wastes, for which further treatment and managing requires additional steps and costs [14]. Besides, it is still difficult to achieve satisfactory removal efficiencies by these methods due to the high solubility of phenol. Hence, there is still a great interest to develop novel technologies for convenient, robust and cost effective treatment of phenol [15].

Advanced oxidation processes (AOPs), which usually operate under room or environmental temperature and pressure [3,16] are based on the generation of strongly oxidizing hydroxyl radicals, $E^{\circ}(HO^{\bullet}, H^{+}/H_2O) = 2.73$ V vs. NHE [17], which may produce more biologically degradable and less toxic substances [18,12]. The photocatalytic process is initiated when a photon with energy ($h\nu$) equal to or higher than the band gap energy (E_g) reaches the photocatalyst, with subsequent formation of electrons (e^-) in the conduction band (CB) and positive holes (h^+) in the valence band (VB) [13]. The so-formed e^-/h^+ pairs can recombine and dissipate the input energy as heat, get trapped in metastable surface states or migrate to the surface in order to react with electron donors and acceptors adsorbed on the semiconductor surface or within the immediate surrounding electrical double layer of the charged particles [19]. Free hydroxyl radicals ($HO^{\bullet}$) are directly produced by reaction of h^+ with H_2O or HO^- at the surface of the catalyst [20]. $HO^{\bullet}$ radicals are extraordinarily reactive, highly unselective species, with rate constant in the order of 10^6–10^9 $M^{-1}\cdot s^{-1}$ and high electrophilicity [3].

A number of papers have been reported on the photodegradation of phenol, most related to the application of modified or doped TiO_2 as photocatalyst [12,13,20–26]. Other photocatalysts such as g-C_3N_4/Fe(III)/persulfate system [27], g-C_3N_4 film [28], α-MnO_2 [29], V_2O_5 [30], iodine doped tin oxide (SnO_2:I) [31], $BiVO_4$ [32], β-$ZnMoO_4$ [33], Co_3O_4 [34], ZnO [35], ZnO/bentonite [1], ZrO_2/Al_2O_3-montmorillonite [36] and Fe-Cu allophane nanoclays [37] have also been explored. The available mechanistic information suggests the photocatalytic transformation of phenol is dependent on most system variables: pH, catalyst composition, catalyst loading, organic substrate concentration, light intensity, electrolyte composition of wastewater, co-solvents, co-oxidant concentration, exciting wavelength and photocatalyst calcination temperature [18].

Clays are inexpensive and widely available and, therefore, attractive substrates for immobilization of a variety of photocatalyst [1,38–43]. Montmorillonite has a large surface area, a good swelling behavior and favorable surface charge characteristics [44–49]. Montmorillonite has a layered structure, with excellent hydrophilic and cation exchange properties. Its layer consists of an octahedral sheet sandwiched between opposing tetrahedral sheets [50]. These layers are stacked by weak dipolar or Van der Waals forces, and have easily modifiable surface and edge charges [51]. Incorporation of the catalyst into the basal space of the layered structure of aluminosilicates clay through the ion exchange intercalation process produce a more reactive clay composite toward the oxidation of organic substrates due to increase of the basal space. The main advantages of intercalation are the proper dispersion of the photocatalyst in solid supports generating distinct reactive sites and less amount of photocatalyst will be required for degradation of organic pollutant [1].

Sulfide semiconducting materials are widely used because of their unique physical, chemical, magnetic, surface electronic and optical properties [52]. Among these, CdS and CuS exhibit versatile applications including photocatalytic hydrogen production, lithium ion batteries, chemical sensors, solar cells, optical materials, solar energy converter, conducting materials, solar radiation absorbers and photocatalysis [52–55]. Cadmium sulfide (CdS) is characterized by a narrow band gap of 2.5 eV, and its valence electron can be easily excited to the conduction band under visible irradiation [56,57]. However, S^{2-} is readily oxidized to SO_4^{2-} by photogenerated holes, and Cd^{2+} ions escape into the solution. A possible way of enhancing the photocatalytic activity of cadmium sulfide is to develop a composite material based on CdS and other semiconductor which is CuS [58]. Copper sulfide (CuS), a typical p-type transition metal sulfide [59], has a narrow band-gap with empty 3p-orbitals in sulfur as a greater electron acceptor. However, CuS has the problem of insufficient long-term stability [55]. Therefore, efforts should concentrate on finding ways to protect these sulfide photocatalysts from photocorrosion.

To protect these materials, we attempt in this work to dope Cd^{2+}-Cu^{2+} mixed sulfides with La^{3+} and incorporate it in montmorillonite clay, with the view that the resulting composite may show better photocatalytic efficiency, with a reduced level of photocorrosion. The supported semiconductor photocatalyst was named mont-La (6%)-$Cu_{0.6}$-$Cd_{0.4}$-S and synthesized using a two-step ion exchange and impregnation method. The characterization of the sample was carried out performing Fourier transform infrared (FTIR), scanning electron microscopy coupled with energy dispersive X-ray spectroscopy (SEM-XEDS), X-ray diffraction (XRD), X-ray fluorescence (XRF) and UV–vis diffuse reflectance spectroscopy (UV–vis DRS), while its photocatalytic activity was evaluated for the degradation of phenol as a model compound. The photoreaction was conducted in an aqueous solution under near UV–vis light at 366 nm wavelength. The effects of various operating parameters such as initial solution pH, initial phenol concentration, catalyst dosage and dissolved oxygen on the rate of photocatalytic degradation and the total organic carbon (TOC) conversion have been investigated. Reaction intermediates produced during the degradation process were detected, and a suitable mechanism is proposed for the degradation of phenol based on HPLC/MS analysis.

2. Experimental

2.1. Materials

Cupric acetate monohydrate ($C_4H_6CuO_4\cdot H_2O$), cadmium acetate dehydrate ($C_4H_6CdO_4\cdot 2H_2O$) and thiourea (NH_2CSNH_2) were purchased from Fluka. Lanthan (III) chloride ($LaCl_3\cdot xH_2O$) was purchased from Merck. Ethylene glycol ($C_2H_6O_2$) was purchased from Prolabo. Phenol (C_6H_5OH), hydrochloric acid (HCl) and sodium hydroxide (NaOH) were obtained from Panreac. Acetonitrile (J.T. Baker) of HPLC grade was used for HPLC analyses. The gases employed were O_2 (purity ≥99.995%) and Ar (purity 99.9992%). All chemicals were used without further purification. Milli-Q water, obtained from a Millipore apparatus with a resistivity of 18.2 MΩ at 298.0 K, and a measured total organic carbon (TOC) ≤5 μg·L^{-1} was used for HPLC purposes. Distilled water was used in all the rest of experiments.

2.2. Catalyst synthesis

In a typical synthesis, a total of 2 mmol of $Cu(OAc)_2$ and $Cd(OAc)_2$ with a Cu:Cd molar ratio of 0.60:0.40, 0.015 mmol of $LaCl_3\cdot xH_2O$ and 6 mmol of thiourea were dissolved into 30 mL of ethylene glycol to form the Cu-Cd-thiourea complex. The montmorillonite clay powder was slowly dispersed into the solution of complex with vigorous stirring, which was continued for 3 h to allow ion exchange to proceed between the complex cations and the exchangeable cations in the clay. The mixture was heated by an oil bath at 160 °C for 2 h. After cooled to room temperature, the samples were centrifuged and washed with distilled water for several times. The

solid was dried at 40 °C and calcined in a microwave oven of 400 W microwave power. The catalyst was noted as mont-La (6%)-$Cu_{0.6}$-$Cd_{0.4}$-S.

2.3. Characterization techniques

The morphology of the samples was recorded using scanning electron microscopy (SEM). SEM images and semiquantitative XEDS microanalyses were taken on a HitachiTM-1000.

Fourier transform infrared spectra were recorded on a FT-IR 6300 spectrometer with KBr as the reference sample. The effective range was from 400 to 4000 cm^{-1}.

The crystalline phases of the resulting materials were determined by powder X-ray diffraction (XRD) using an X'pert Pro PANanalytical polycrystal diffractometer with a X'celerator RTMS detector and nickel-filtered Cu Kα radiation (λ = 1.5406 Å) operated at a current of 40 mA and a voltage of 40 kV. The samples were scanned at step size of 1°/min over a range of 4–90° covering the main diffraction peaks of the clay, CdS and CuS nanocrystals.

Composition of the catalyst before and after its use was tested by semiquantitative X-ray fluorescence on S4 Pioneer Bruker X-ray spectrofluorimeter.

UV–vis diffuse reflectance spectra (DRS) of the catalyst and the montmorillonite clay samples were performed with a UV-Vis-NIR Varian Cary 5000 spectrometer with double beam and double shutter, synchronized electronically, equipped with a Labsphere diffuse reflectance accessory at room temperature. $BaSO_4$ powder is used as a standard for baseline measurements and spectra are recorded in the wavelength range of 200–800 nm.

2.4. Photocatalytic activity

Photocatalytic activity of the catalyst was assessed by photodegradation of phenol solutions in a Pyrex immersion glass photoreactor with axial geometry. The reactor was equipped with a medium-pressure Hg-vapor lamp, with intense emission lines at λ_{exc} = 254, 313, 366, 405, 436, 546 and 578 nm, located axially in the reactor inside a glass immersion tube. The UV lines at λ_{exc} < 366 nm were filtered out using a DURAN 50® glass jacket filled with water, limiting the irradiation to near UV–vis (NUV–vis).

In all the experiments, 200 mL aqueous phenol solution with the required concentration of phenol, containing appropriate quantity of the photocatalyst was used. Initial pH of the solution was adjusted to a required value by adding 0.1 M NaOH or 0.1 M HCl. Aqueous phenol solution was magnetically stirred. A similar experiment was carried out in the absence of light. Photolysis was also evaluated under UV and NUV–vis radiation without catalyst. All the experiments were run for 4 h. At regular time intervals, 3 mL samples were withdrawn and filtered through Sartorius NY 0.45 μm filters before analysis. All kinetic runs were carried out at 298.0 K, the temperature being kept by water flow from a thermostat-cryostat.

The photocatalytic degradation efficiency was calculated based on the initial phenol concentration. The change in phenol concentration was monitored by measuring the change in UV–vis absorbance at 270 nm using a Biochrom Libra S 70 spectrophotometer, and also by HPLC in a Thermo Fisher with a UV 6000 LP detector at 210 and 270 nm and AS 3000 autosampler and a P4000 solvent pump; the stationary phase consisted in a col KROMAPHASE C18 column (4.6 mm × 150 mm × 5 μm), injected volume 50 μL, column temperature of 30 °C and a flow of mobile phase acetonitrile:water (25:75, v/v) at a flow rate of 1.0 mL·min^{-1}.

Identification of the photoproducts was carried out by HPLC/MS, using a Thermo Scientific, LTQ Orbitrap Discovery apparatus, equipped with an electrospray interface operating in negative ion mode (ESI−). A Phenomenex Kinetex XB-C18 (100 mm × 2.10 mm, 2.6 μm) column was used, operated at 30 °C with the elution solvents A (aqueous 0.1% formic acid) and C (methanol 0.1% formic acid) and a flow-rate of 200 μL·min^{-1}. The gradient is described as follows: 0–1 min, 95–95% A and 5–5% C; 1–8 min, 95–5% A and 5–95% C; 8–10 min, 5–5% A and 95–95% C; 10–11 min, 5–95% A and 95–5% C; 11–15 min, 95–95% A and 5–5% C. The injection amount was 5–25 μL. The analyses were carried out using full-scan data dependent MS scanning from m/z 50 to 500.

Total organic carbon (TOC) was quantified using a Shimadzu TOC-5000A analyzer. The TOC removal efficiency was calculated based on its initial value.

2.5. Photodegradation kinetics

UV–vis photocatalytic degradation processes can be adequately described using a modified Langmuir–Hinshelwood kinetic model [46], as in Eq. (1) [60]:

$$r = k_{LH} \cdot \Theta = k_{LH} \cdot \frac{K_{LH} \cdot C}{1 + K_{LH} \cdot C} \quad (1)$$

where C is the phenol concentration once the adsorption equilibrium has been established, k_{LH} (mol s^{-1} cm^{-2}) is an apparent kinetic rate constant per unit of surface area, and Θ (cm^2) accounts for the coverage of catalyst surface by phenol. K_{LH} is the Langmuir–Hinshelwood adsorption constant. Assuming $K_{LH} \cdot C \ll 1$ (see Section 3.2), Eq. (1) reasonably reduces to a first order kinetic model (Eq. (2)):

$$r = k_{app} \cdot C \quad (2)$$

where

$$k_{app} \approx k_{LH} \cdot K_{LH} \quad (3)$$

is the limiting apparent pseudo-first order kinetic rate constant when $K_{LH} \cdot C \ll 1$.

Since heterogeneous photocatalysis depends on the initial concentration of the organic substrate [46], $[phenol]_0$ was kept constant at 20 mg·L^{-1} (=0.21 mM) except when studying the effect of its concentration.

3. Results and discussion

3.1. Characterization of the catalyst

3.1.1. SEM

The morphology and elemental analysis of the montmorillonite reference clay (mont-Na) and mont-La (6%)-$Cu_{0.6}Cu_{0.4}S$ catalyst were studied by scanning electron microscopy (SEM), and the corresponding SEM images are presented in Fig. 1a and b. The morphologies of both mont-Na and mont-La (6%)-$Cu_{0.6}Cu_{0.4}S$ are quite similar. The shape of clay particles does not change upon introduction of the sensitizing material, suggesting that La, CdS and CuS deposition do not alter the clay structure.

Typical XEDS spectra obtained from the clay and the material are shown in Fig. 1c and d. In the spectra, peaks associated with Al, Si, Fe, Mg, Na, Cd, Cu and S were observed. Al, Si, Fe, Mg and Na peaks resulted from montmorillonite, and weak signals of Cd, Cu and S in the XEDS are consistent with the low content of CdS and CuS in the composite. No signal from La species can be observed in the XEDS patterns, same as the crystal phases attributed to CdS, CuS and La. This is due to the very low concentration of La on the mont-$Cu_{0.6}Cu_{0.4}S$, and is possibly an evidence of the high dispersion of La in the composite.

3.1.2. FTIR analysis

Fig. 2 shows the FTIR spectra of the montmorillonite clay and the mont-La (6%)-$Cu_{0.6}Cd_{0.4}S$ catalyst, where the stronger absorp-

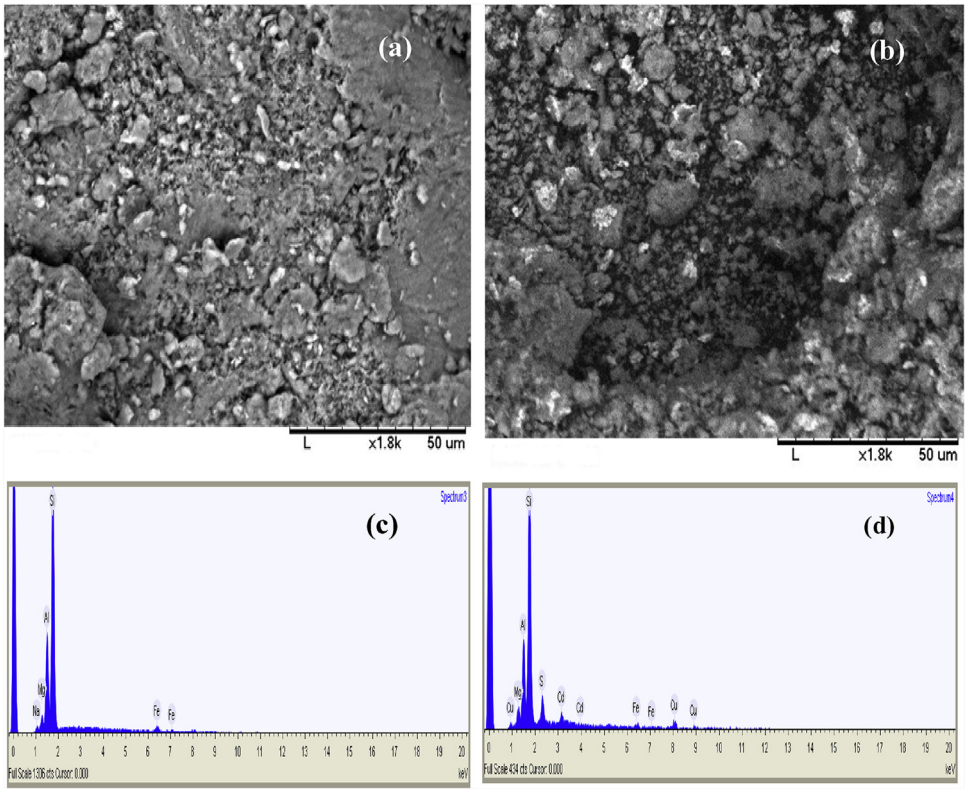

Fig. 1. SEM images (accelerating voltage = 15 kV, magnification = 1800, emission current = 87,400 nA) and XEDS analysis of mont-Na (a, c) and mont-La (6%)-$Cu_{0.6}Cd_{0.4}S$ (b, d).

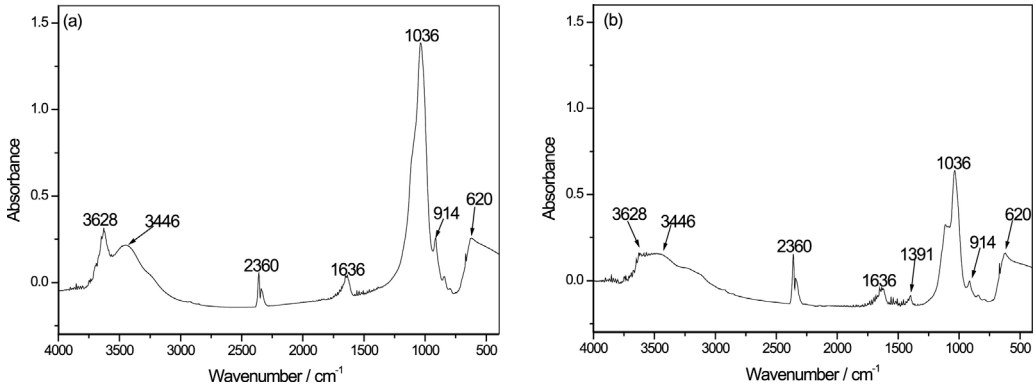

Fig. 2. FTIR spectra of (a) mont-Na and (b) mont-La (6%)-$Cu_{0.6}Cd_{0.4}S$.

tion band centered at 3628 cm^{-1} is ascribed to OH stretching mode in Al\Al\OH, characteristic of montmorillonite [61,62]. The broad absorption band located at 3446 cm^{-1} corresponds to the vibration of physisorbed water on the surface of the clay [61,63]. The observed peak band at 2360 cm^{-1} is attributed to O—H from H_2O and CO_2 adsorbed on the surface grains while handling the sample under room atmosphere [64]. The peak at 1636 cm^{-1} is assigned to the bending vibration mode of O—H in adsorbed water molecules [65–67]. The intense band at 1036 cm^{-1} can be attributed to Si—O—Si asymmetric stretching vibration from clay [66]. The peak observed at 914 cm^{-1} is due to the hydroxide (OH) deformations linked to Al and/or Mg ions [62]. Also, the peak in 620 cm^{-1} is related to the stretching vibrations of tetrahedral atoms in montmorillonite [66].

The FTIR spectra reveal that the as-prepared mont-La (6%)-$Cu_{0.6}Cd_{0.4}S$ sample presents the same absorption bands as the clay reference, indicating that the montmorillonite structure remained almost unchanged after treatment. Comparison of the FTIR spectra of mont-La (6%)-$Cu_{0.6}Cd_{0.4}S$ with montmorillonite, shows an additional peak at about 1391 cm^{-1} in the FTIR spectrum of mont-La (6%)-$Cu_{0.6}Cd_{0.4}S$ nanocomposite, indicating the formation of CdS and CuS in this catalyst. This result is in good agreement with previous observations [61].

3.1.3. XRD

To determine the crystal phase composition of the prepared nanocomposites, XRD measurements were carried out at room temperature for the diffraction angle ranging from 6° to 90°. The XRD patterns of the mont-Na and mont-La (6%)-$Cu_{0.6}$-$Cd_{0.4}$-S nanocomposite were shown in Fig. 3.

The XRD pattern of the nanocomposite shows a measurable basal (001) peak. The presence of this peak confirms that the composite retained the layered structure of the parent clay indicating that the montmorillonite did not change after deposition of CdS

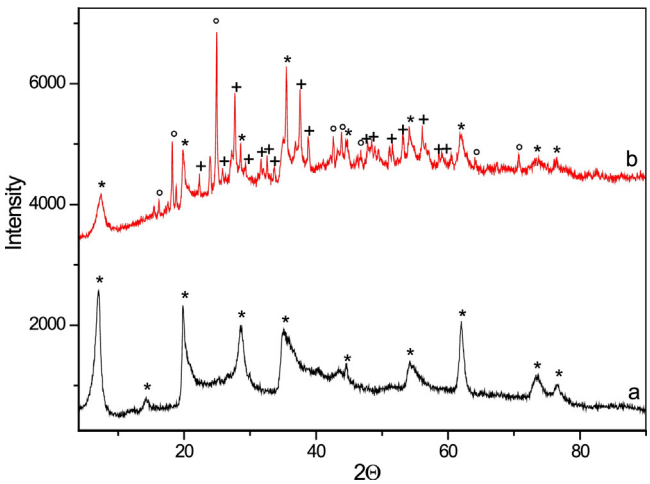

Fig. 3. XRD patterns of mont-Na (a) and mont-La (6%)-$Cu_{0.6}$-$Cd_{0.4}$-S (b): (*) montmorillonite, (+) CuS and (°) CdS.

and CuS. This composite have larger basal spacing, d_{001}, than that of the corresponding reference clay. This expansion of the basal spacing can be ascribed to CdS and CuS insertion into the intergallery spaces of montmorillonite. All mentioned diffraction peaks for the original montmorillonite can also be observed for the mont-La (6%)-$Cu_{0.6}$-$Cd_{0.4}$-S composite. The positions of the diffraction peaks are basically unchanged as compared with the reference (montmorillonite).

As for montmorillonite clay (diffraction pattern (a)), the characteristic peaks are found at 7.12°, 14.24°, 19.82°, 28.60°, 35.12°, 44.64°, 54.21°, 61.99°, 73.64° and 76.55°.

From diffraction pattern (b), it can be established that the catalyst sample reveals a mixture of crystalline phases corresponding to CdS and CuS. The main peaks located at 16.19°, 18.20°, 23.94°, 25.01°, 42.59°, 43.84°, 46.75°, 64.27° and 70.75° were assigned to the hexagonal structure of CdS. Similarly, hexagonal CuS was found to exhibit peaks located at 2θ at 22.40°, 25.78°, 27.79°, 29.32°, 31.64°, 32.72°, 33.63°, 37.64°, 38.86°, 47.96°, 48.41°, 51.34°, 53.19°, 56.12°, 58.88° and 59.35°, in good agreement with the literature [55,59,68]. The intense and sharper diffraction peaks indicated the high crystallinity of the catalyst and must be due to a high proportion of CdS and CuS in the outer layers of clay, as the very small nanoparticles intercalated in the montmorillonite layers are not expected to show such diffractions.

In mont-La (6%)-$Cu_{0.6}$-$Cd_{0.4}$-S sample no diffraction peaks corresponding to La-phases were detected, indicating that its weight percentage is too small. Again, it is interpreted as a sign of high dispersion of La species.

3.1.4. UV visible DRS

The optical properties of the mont-La (6%)-$Cu_{0.6}$-$Cd_{0.4}$-S nanocomposite and the reference montmorillonite clay were measured using UV–vis diffuse reflectance spectroscopy and the results are shown in Fig. 4. From Fig. 4a, it can be clearly seen that the montmorillonite clay shows absorption spectrum in the UV region between 200 and 350 nm while the catalyst sample show also absorption spectrum in the visible region from 550 to 800 nm.

The montmorillonite shows an absorption maximum at the wavelength of 255 nm, the absorbance of light by montmorillonite in the UV–vis region is generally attributed to the electronic transitions of the different transition metals within the lattice or intergallery of the clay.

After incorporation of La (6%)-$Cu_{0.6}$-$Cd_{0.4}$-S in the clay, this maximum shifted slightly to 259 nm and another peak appeared at 215 nm. In addition, a broad band extending into the region 550–800 nm was also observed in the catalyst spectrum. According to [59], the wide peak observed at longer wavelengths in the range of 700–900 nm is characteristic of covellite CuS, while [69] explain it by the d-d transition of Cu^{2+}.

The band gap energy values were estimated using the Kubelka–Munk function ($F(R)$) and Tauc plot of $(F(R)\cdot E)^{1/2}$ versus photon energy ($h\nu$) (Fig. 4b). The band gaps estimated from the intercepts of the tangents to the plot are 3.36 eV and 2.11 eV for the catalyst and the reference clay, respectively. There was a reduction in the band gap energy of mont-La (6%)-$Cu_{0.6}$-$Cd_{0.4}$-S as compared to mont-Na and for this reason, lower photon energy was required for photo-activation of mont-La (6%)-$Cu_{0.6}$-$Cd_{0.4}$-S. These results suggested that the catalyst could be a promising photocatalytic material absorbing the visible light.

3.2. Effect of NUV–vis irradiation

Fig. 5 shows the adsorption, photolysis and photocatalytic degradation of phenol upon NUV–vis irradiation.

Under dark conditions, and in the presence of 1 g·L^{-1} mont-La (6%)-$Cu_{0.6}$-$Cd_{0.4}$S ca. 9% removal was observed after 4 h from a 20 mg·L^{-1} phenol aerated solution at its natural pH (ca. 5.4) (Fig. 5), which is attributed to the adsorption of phenol onto the catalyst. The rate constant for adsorption was estimated as $k_{Ads} \approx 0.056\ min^{-1}$ ($t_{1/2} \approx 12.3$ min).

As shown in Fig. 5, the direct NUV/vis photolysis of phenol, without any catalyst, led to a very low phenol phototransformation, only 9% of phenol reduction after 4 h irradiation. This is explained in terms of a low phototransformation quantum yield, i.e., the reactive

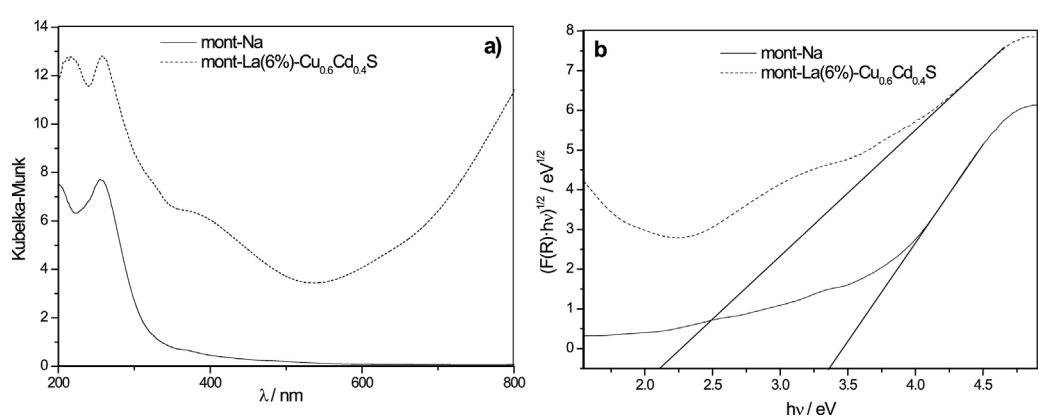

Fig. 4. (a) UV–vis DRS in Kubelka–Munk mode and (b) Tauc plots for determination of band gap values for mont-Na and mont-La (6%)-$Cu_{0.6}Cd_{0.4}S$ using Kubelka–Munk function.

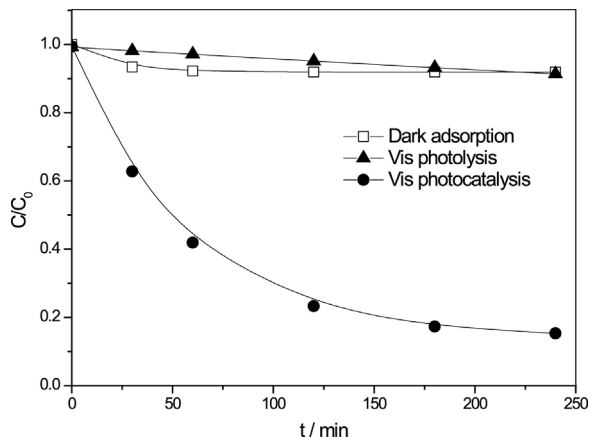

Fig. 5. Evolution of [phenol] upon dark adsorption (□), NUV/vis photolysis (▲) and NUV/vis photocatalysis (●). $[Phenol]_0 = 20\,mg{\cdot}L^{-1}$; [catalyst] = 1.0 g·L^{-1}; pH = 5.4; $P(O_2) = 21\%$; $T = 298.0\,K$.

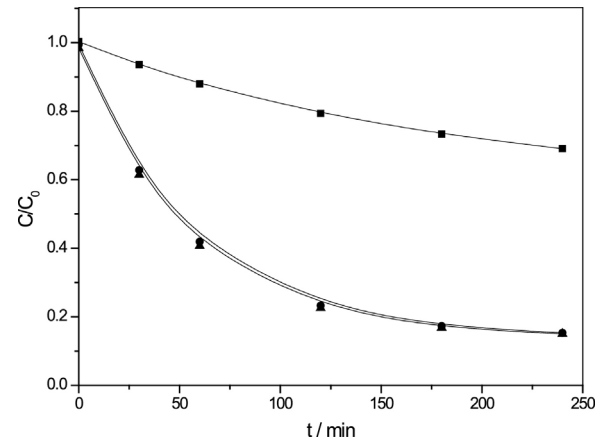

Fig. 6. Evolution of phenol concentration at different oxygen percentages under near UV visible irradiation. $[Phenol]_0 = 20\,mg{\cdot}L^{-1}$; [catalyst] = 1.0 g·L^{-1}; pH = 5.4. ■ 0% O_2; ♦ 21% O_2; ▲ 100% O_2; $T = 298.0\,K$.

excited states deactivate through non-photochemical processes. It also implies that direct photolysis is not a suitable method to degrade/reduce phenol and phenol derivatives in water. In line with these results, Chun et al. [70] observed 4% phenol degradation in 60 min using $\lambda_{irradiation} > 330$ nm, or those of Shet and Vidhya [21] who found ca. 14% degradation after 360 min with solar light at 33 °C. Ling et al. [13] found that only 3% of phenol was transformed after 24 h of UV irradiation and similar low conversions were observed by Poulopoulos et al. [71], Dang et al. [72] and Naeem and Feng [73]. In this case the observed initial rates (r_0) of photolysis were $r_{0,NUV/vis} = 5.2 \times 10^{-3}\,mg{\cdot}L^{-1}{\cdot}min^{-1}$.

Irradiation of the mont-La (6%)-$Cu_{0.6}Cd_{0.4}S$ photocatalyst with NUV–vis light strongly enhanced the transformation to 86% after 4 h (Fig. 5), with $k_{NUV-vis-photocat} \approx 0.019\,min^{-1}$ ($t_{1/2} \approx 36.8$ min). Since $k_{Ads} \gg k_{NUV-vis-photocat}$ replacement of adsorbed molecules after photocatalysis reaction takes place favorably.

These results reflect the potential of mont-La (6%)-$Cu_{0.6}$-$Cd_{0.4}$-S to harvest light in the NUV/vis region, so that the yield of HO• available for phenol removal is higher (Eqs. (4)–(6)). Hydrogen abstraction yields a phenoxyl radical (Eq. (7)), that then reacts with dissolved $^3O_2$ to yield peroxyl radical species that further react, leading finally to CO_2/CO_3^{2-} and water (Eq. (8)). [13]

$$\text{mont-La(6\%)-Cu}_{0.6}\text{Cd}_{0.4}\text{S} + h\nu \rightarrow e^-_{CB} + h^+_{VB} \quad (4)$$

$$h^+_{VB} + OH^-_{ads} \rightarrow HO^\bullet_{ads} \quad (5)$$

$$h^+_{VB} + H_2O_{ads} \rightarrow HO^\bullet_{ads} + H^+ \quad (6)$$

$$HO^\bullet + C_6H_5OH \rightarrow C_6H_5O^\bullet + H_2O \quad (7)$$

$$C_6H_5O^\bullet + O_2 \rightarrow \text{Intermediates} \rightarrow\rightarrow\rightarrow CO_2/CO_3^{2-} + H_2O \quad (8)$$

3.3. Effect of operational parameters under NUV–vis

3.3.1. Effect of dissolved oxygen

The results obtained from the study of the influence of oxygen on the degradation are shown in Fig. 6. Photodegradation is slower in the absence of O_2, when pure Ar is bubbled through the suspension. The residual transformation observed in these conditions is due to the residual amount of both O_2 remaining adsorbed onto the catalyst, and adsorbed phenol reacting with HO• and e$^-$.

The enormous increase in photodegradation between 0% O_2 and 21% O_2 is due to the higher production of HO• and $O_2^{\bullet-}$ responsible for degradation of phenol (lower degree of e$^-$/HO• annihilation). The percentages of degradation with 21% and 100% O_2 are similar. No increase in the photodegradation is observed when pure oxygen is bubbled through the suspension. This can be attributed to having reached the optimal adsorption of O_2 on the surface of the catalyst that may also inhibit adsorption of phenol molecules at the active sites of the catalyst. Similar results were obtained in the literature [70,74], as well as with other organic compounds [60,75]. The first-order apparent rate constant for the reaction with 0% O_2 was 0.006 min^{-1} while for 21% and 100% O_2 a k_{app} of 0.019 min^{-1} was obtained.

On the photocatalyst, oxygen as electron acceptor provides a natural sink for photo-generated electrons. Thus, hydroxyl ions (HO^-) and water molecules adsorbed on the surface of the catalyst are traps for holes resulting in the formation of hydroxyl radicals (HO•) via Eqs. (4)–(6) that are the major way of photogeneration of HO• radicals. Adsorbed O_2 traps e$^-$, resulting in formation of superoxide species, $O_2^{\bullet-}$, and its conjugate acid, hydroperoxide, $HO_2^\bullet$ (Eqs. (8) and (9)). Hydrogen peroxide can be produced via Eq. (10) and further react to form HO• radicals (Eq. (11)). Phenol may undergo either an electron from the aromatic ring (or more likely from the –OH group) to the strongly oxidizing HO•, to yield a phenoxyl radical, or a hydrogen abstraction by HO• to yield a carbon-centered radical that may transform into a phenoxyl radical. The reactivity of the so-generated intermediates could lead (by the action of oxygen) to a phenol-hydroxyl derivative, unstable enough to keep reacting through successive oxidations, with eventual ring opening and decomposition all the way through into CO_2 and H_2O (Eqs. (7) and (8)). [72]

$$e^- + O_{2,ads} \rightarrow O_2^{\bullet-} \quad (9)$$

$$O_2^{\bullet-} + H^+ \rightarrow HO_2^\bullet \quad (10)$$

$$O_2^{\bullet-} + H^+ + HO_2^\bullet \rightarrow H_2O_2 + O_2 \quad (11)$$

$$H_2O_2 + h\nu \rightarrow 2HO^\bullet \quad (12)$$

3.3.2. Effect of catalyst loading

The optimum weight of catalyst is an important parameter to be investigated to avoid ineffective excess of catalyst and to ensure the total absorption of efficient photons. To study the effect of catalyst loading on phenol degradation, experiments were conducted with different catalyst loadings: 0.5, 0.8, 1.0, 1.2 and 1.5 g·L^{-1} at 20 mg·L^{-1} initial phenol concentration, at natural pH (ca. 5.4).

Fig. 7b shows that increasing amounts of catalyst loads have no significant effect on the degradation rate of phenol, that remains constant, with $k_{app} = 0.01968\,min^{-1}$ ($t_{1/2} = 35.1$ min), 0.01448 min^{-1} ($t_{1/2} = 47.6$ min), 0.01881 min^{-1} ($t_{1/2} = 36.7$ min), 0.01556 min^{-1} ($t_{1/2} = 44.3$ min), and 0.01672 min^{-1} ($t_{1/2} = 41.3$ min), for initial catalyst concentrations

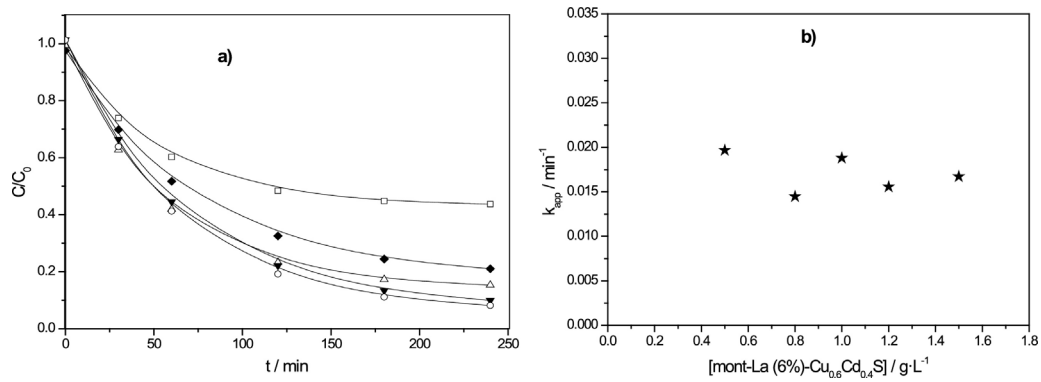

Fig. 7. Influence of catalyst load: (a) evolution of phenol concentration at different catalyst concentrations under NUV–vis irradiation (□ 0.5 g L^{-1}; ♦ 0.8 g L^{-1}; △ 1 g L^{-1}; ▼ 1.2, ◯ 1.5 g L^{-1}); (b) dependence of the rate constant with the catalyst load. [Phenol]$_0$ = 20 mg·L^{-1}; $P(O_2)$ = 21%; pH = 5.4; T = 298.0 K.

of 0.5 g·L^{-1}, 0.8 g·L^{-1}, 1 g·L^{-1}, 1.2 g·L^{-1} and 1.5 g·L^{-1}, respectively. Instead (Fig. 7a), an increase in the amount of catalyst improves by ca. 40% the extent to which phenol disappears. This can be attributed to a larger number of active sites for generation of more radicals.

According to the obtained results, the amount of catalyst was kept constant at 1.0 g·L^{-1} in all the rest of photocatalysis experiments.

Within the range of catalyst concentrations used, no decrease in the rate was observed. Typically, photocatalyzed degradation of phenol shows an optimal catalyst loading [76]. Usually, the effect opacity of the solution becomes more important than the increase in the number of reactive sites. However, we did not observe this. The fact that the rate constant does not change with the load of catalyst can be explained by a combination of effects: an increase in the amount of catalyst provides an increased number of active sites for adsorption; however, the simultaneous increase in solution opacity causes a decrease in the penetration of the photon flux, thus here there is a balance between these two opposing effects.

3.3.3. Effect of initial phenol concentration

The effect of initial phenol concentration was investigated varying the concentration from 10 to 50 mg·L^{-1}, as shown in Fig. 8. The transformation rate decreased as the initial phenol concentration increased. The extent of reaction in 240 min decreased from ca. 90% for 10 mg L^{-1} phenol to 63% for 50 mg L^{-1} phenol (Fig. 8a), and the apparent rate constants obtained were 0.02076 min^{-1} ($t_{1/2}$ = 33.4 min), 0.01881 min^{-1} ($t_{1/2}$ = 36.9 min), 0.01246 min^{-1} ($t_{1/2}$ = 55.6 min), 0.01122 min^{-1} ($t_{1/2}$ = 61.8 min), and 0.01048 min^{-1} ($t_{1/2}$ = 66.1 min), for initial concentrations of phenol of 10 mg·L^{-1}, 20 mg·L^{-1}, 30 mg·L^{-1}, 40 mg·L^{-1} and 50 mg·L^{-1}, respectively.

These results are similar to those obtained by several authors, up to a certain initial concentration of phenol; the first order rate constant decreases as [phenol]$_0$ increases. [71,73,76,77] in the degradation of phenol, at pH 5.0, photocatalyzed by microwave irradiated zinc oxide found such decrease in reaction rate with the initial phenol concentration irrespective of the radiation source (sunlight, visible and UV light). Similar behavior was also observed by [74] using TiO_2, who found that the pseudo first-order reaction rate constant is inversely proportional to the initial concentration of phenol only when the concentration is above a critical value (30 mg L^{-1}). This is explained by the competition between phenol molecules and HO^- for the same adsorption sites [74].

Our results are consistent with previous observations [11,20,21,35,78,79], indicating that photocatalytic degradation is rather promising at lower reactant concentrations. Fabiano de Almeida et al. [22] reported that 50 mg·L^{-1} initial concentration of phenol was degraded in 360 min with k_{app} = 0.0114 min^{-1} (phenol by HPLC-DAD) and 0.0040 min^{-1} (TOC), corresponding to half-lives ($t_{1/2}$) of 60.8 min (phenol by HPLC-DAD) and 248.4 min (TOC) using 1 g·L^{-1} of TiO_2/MgZnAl-5 using a 125 W mercury vapor lamp. Therefore, one can conclude that the mont-La (6%)-$Cu_{0.6}$-$Cd_{0.4}$-S composite photocatalyst showed an adequate kinetic behavior with the potential to eliminate phenolic compounds in aqueous media.

3.3.4. Effect of pH value of phenol aqueous solution

The pH value of the solution has a relevant effect on the photocatalytic reaction because the semiconductor's surface state of protonation, its potential of zero charge, and the dissociation of phenol are all strongly pH dependent. When pH < pK_a value, phenol exists as a neutral species (C_6H_5OH), whereas when pH > pK_a phenoxide ion ($C_6H_5O^-$) is present. Surface charge promotes or inhibits coulombic interactions during adsorption, thus favoring/inhibiting the interaction between catalyst and pollutant, something well-known for a variety of photocatalysts [11,20,35,78,80].

In this work, pH was varied in the range (3.0–12.0) with initial phenol concentration of 20 mg·L^{-1} and 1.0 g·L^{-1} of mont-La (6%)-$Cu_{0.6}Cd_{0.4}S$ catalyst load, to study its effect. As shown in Fig. 9a, the efficiency of the photocatalytic degradation of phenol depends on the acidity of the medium. Phenol removal is better at acidic pH = 3 with a removal percentage around 91% after 240 min. As pH increases, the extent of removal decreases, with a reduction up to 59% at pH = 12. Same behavior was found by Shet and Vidhya [21] in the solar light mediated photocatalytic degradation of phenol using Ag core–TiO_2 shell (Ag@TiO_2). In fact a general feature of the photocatalyzed degradation of phenol and substituted derivatives is the increase of its removal as pH goes from acid conditions to neutral and then the decrease as the medium becomes alkaline [1,11,20,21,35,74,78,81]. Such behavior is related to the relative states of protonation of the surface of catalyst and phenol. Phenol has a pK_a = 9.98, [82], while montmorillonite shows an isoelectric point somewhere around 5 [83], that can be assumed to be very similar to that of our catalyst discussed here, as clay is the main component of the catalyst. As pointed by [74] at low pH the surface of TiO_2 is occupied with H^+ ions, therefore the generation of $HO^\bullet$ radicals is slowed down. As pH increases the protonation of the surface decreases and as in pH < 9 most of the phenol remains undissociated (C_6H_5OH), the maximum number of phenol molecules are adsorbed on the surface and photodegradation is enhanced. In an alkaline medium, both the surface and phenol, as $C_6H_5O^-$, are negatively charged, they repel away, and as a result phenol degradation decreases. Fig. 9b shows the effect of pH on the apparent first order rate constant determined using the Langmuir–Hinshelwood model. The photoefficiency of the process

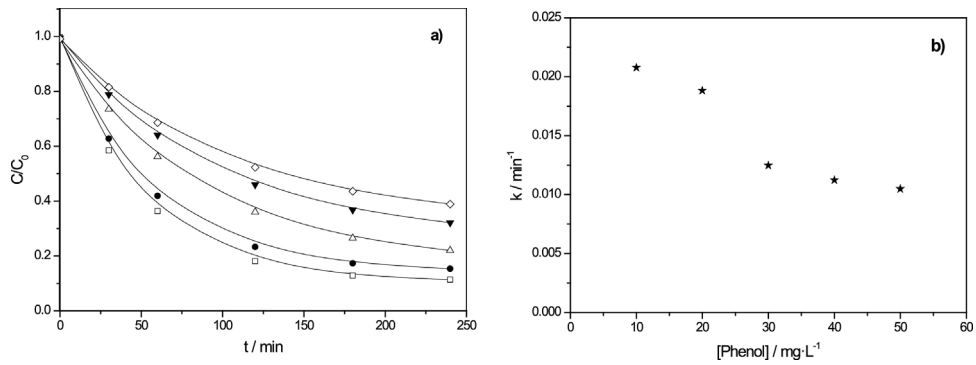

Fig. 8. Effect of initial phenol concentration: (a) phenol decay at different concentrations under near UV visible irradiation. [catalyst] = 1 g L^{-1}; $P(O_2)$ = 21%; pH = 5.4. □ 10 mg·L^{-1}; ● 20 mg·L^{-1}; △ 30 mg·L^{-1}; ▼ 40 mg·L^{-1}; ◊ 50 mg·L^{-1}; (b) dependence of the rate constant for phenol decay with the initial concentration of phenol, T = 298.0 K.

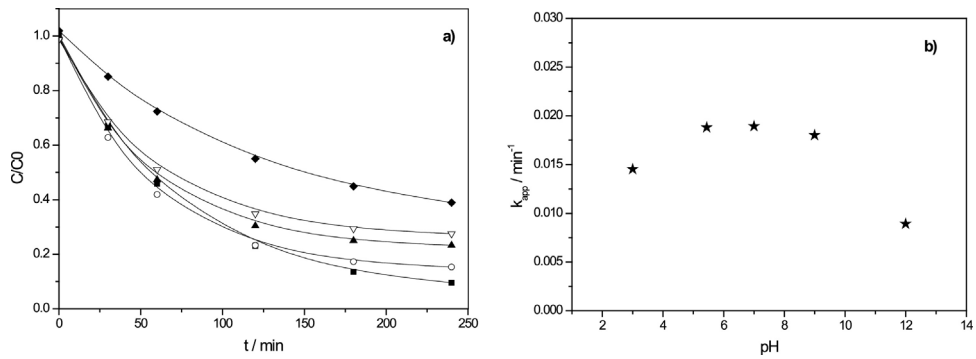

Fig. 9. Effect of pH: (a) evolution of [phenol] at different pHs upon NUV–vis irradiation; pH = 3 (■), 5.44 (nat, ○), 7 (▲), 9 (▽), 12 (♦); (b) dependence of k_{app} with the pH of the medium. $[Phenol]_0$ = 20 mg·L^{-1}; $P(O_2)$ = 21%; [catalyst] = 1 g·L^{-1}; T = 298.0 K.

increases at pH > 3 (k_{app} = 0.015 min^{-1}), gets is maximum value at pH 5–9 (k_{app} = 0.018 min^{-1}) and decreases at higher pH, where phenol removal becomes slower (at pH = 12, k_{app} = 0.009 min^{-1}), i.e., optimal intermolecular interaction takes place when the surface is protonated and phenol is neutral.

3.4. Total organic carbon

In order to determine the degree of mineralization reached upon photocatalysis, two samples in each test were collected at the beginning of the experiment and after 4 h of photo irradiation and then analyzed for TOC concentration. Fig. 10 presents the TOC removal results on the photocatalytic degradation of phenol. A concentration of 20 mg·L^{-1} phenol with measured TOC value of 17.7 mg·L^{-1} was applied in this study. It was observed that the TOC values for the photocatalytic activity in the presence of mont-La (6%)-$Cu_{0.6}Cd_{0.4}S$ catalyst under NUV–vis light irradiation drastically decreased from 17.7 to 3.93 mg·L^{-1} during 240 min of irradiation, which means 77.8% TOC removal (Fig. 10a). The lager extent of TOC removal by mont-La (6%)-$Cu_{0.6}Cd_{0.4}S$ points to a higher activity of the catalyst under NUV–vis light to provide oxidizing species for the photo-mineralization process. After 240 min of irradiation, complete photomineralization of phenol by heterogeneous photocatalysis with mont-La (6%)-$Cu_{0.6}Cd_{0.4}S$ was not achieved, suggesting the formation of persistent intermediates which resist photocatalytic activity.

After 4 h of NUV–vis light photocatalysis, virtually 84% TOC content was eliminated in oxygenated solutions, in accordance with the degradation of phenol and its intermediates within this treatment interval (Fig. 10b). Although phenol molecules could not be detected in solutions purged with argon, nearly 28% of the initial TOC content of the solution was detected even after 4 h of treatment.

Similarly, variations in the initial pH also led to reduction of the final TOC conversion after 4 h from 80.8% (pH = 3) and 77.8% (no pH variation) to 59.7% (pH = 9) (Fig. 10c). Solís et al. [81] showed the variation in initial pH affect TOC removal.

3.5. Mechanism of photocatalyzed degradation

The degradation of phenol involves complicated multistage processes [5,84]. It has been demonstrated that the degradation process with catalyst is energetically favorable for the decomposition of phenol and that two types of oxidizing species: HO• hydroxyl radicals and h^+ are involved in the transformation of aromatic compounds. However, the life spans of the intermediates formed at different stages of the reaction are short, either because the intermediates can undergo further fast catalytic oxidation [84], or because of their ability to avoid reaction with photoactive species or to poison the surface.

For determination of phenol intermediates, HPLC tandem MS was used. Fig. 11 shows a typical HPLC chromatogram. HPLC and MS data are summarized in Table 1. Because of the low concentrations of photoproducts, fortification of the samples by co-injection of references would strongly alter our experiment. Therefore, identification of the proposed products is based on the obtained MS, as compared to those in databases. The main intermediates identified in this way were: **(1)** pyrocatechol, resorcinol and/or hydroquinone, **(2)** hexa-2,4-dienedioic acid, **(3)** penta-2,4-dienoic acid, **(4)** carbonic acid, **(5)** penta-2,4-dienal, **(6)** pent-2-enoic acid, **(7)** pent-2-enal, **(8)** 3-hydroxypropyl acid, **(9)** hex-2-enedioic acid, **(10)** biphenyl, **(11)** (2-hydroxyphenyl)(phenyl)methanone and **(12)** 9H-

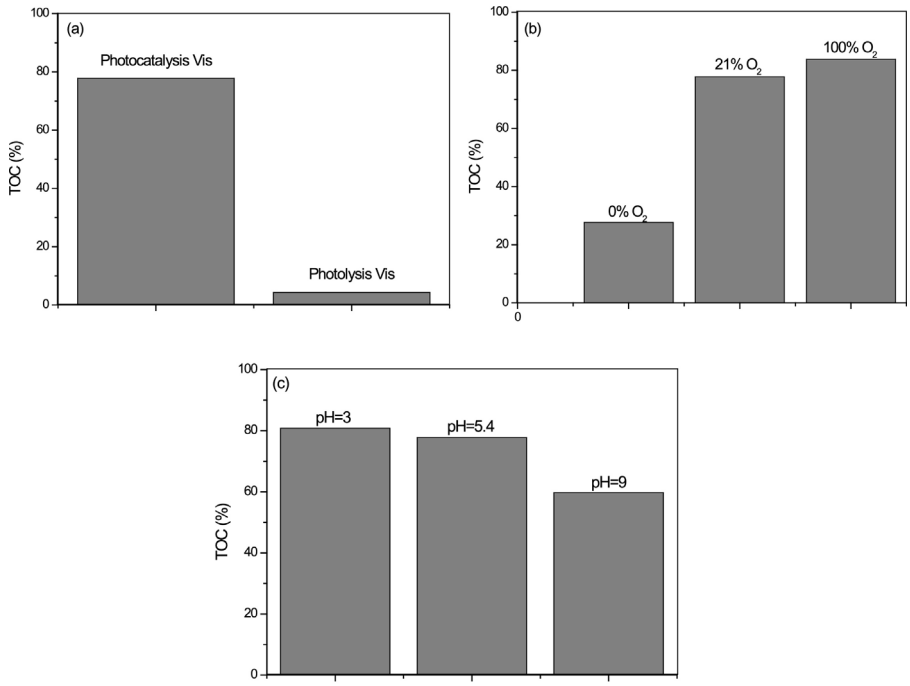

Fig. 10. Effect of irradiation source (a), dissolved oxygen (b) and pH solution (c) on TOC removal for phenol photocatalyzed degradation. $[\text{Phenol}]_0 = 20\ \text{mg}\cdot\text{L}^{-1}$; $T = 298.0$ K.

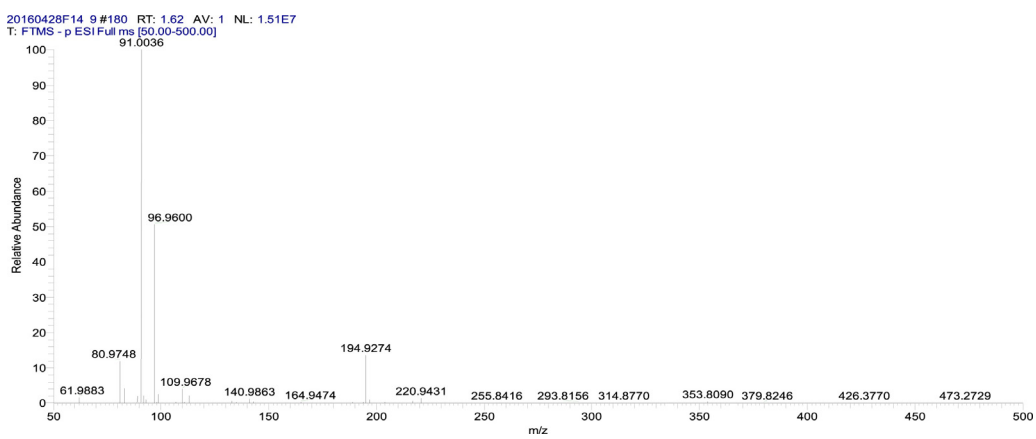

Fig. 11. HPLC–MS chromatogram of phenol photoproducts.

Table 1
HPLC–MS data of phenol photoproducts.

Compounds	$[M-H]^-$ (m/z)	t_R (min)
(1) pyrocatechol, resorcinol and/or hydroquinone	109.9678	1.70
(2) (2Z,4Z)-hexa-2,4-dienedioic acid	140.9863	1.50
(3) (Z)-penta-2,4-dienoic acid	96.9600	1.46
(4) carbonic acid	61.9883	1.45
(5) (Z)-penta-2,4-dienal	80.9748	1.44
(6) (Z)-pent-2-enoic acid	98.9557	1.58
(7) (Z)-pent-2-enal	82.9719	1.43
(8) 3-hydroxypropyl acid	89.0245	1.67
(9) hex-2-enedioic acid	142.9656	1.52
(10) biphenyl	152.9253	1.04
(11) (2-hydroxyphenyl)(phenyl)methanone	196.9233	1.49
(12) 9H-xanthen-9-one	194.9275	1.53

xanthen-9-one. That is, degradative routes into smaller molecules are found, but also routes leading to higher MW transformation products.

Phenol transformation is described by the reaction mechanism shown in Fig. 12. HO• radical attacks the phenyl ring, yielding intermediate **(1)**. In a degradative pathway, hydroxylation with hydrogen addition and opening of the phenyl ring gives **(2)**, which leads to intermediate **(3)** and **(4)** by C—C bond breaking, hydroxylation and hydrogen addition. **(3)** gives **(5)** by dehydroxylation and hydrogen addition, leading to **(7)** by addition of hydrogen. **(3)** may also yield **(6)** by hydrogen addition, leading to **(7)** by dehydroxylation and hydrogen addition, or to **(8)** through C—C scission and reaction with water. Alternatively, **(2)** may undergo decarboxylation, dehydroxylation and hydrogen addition to yield **(5)**. **(2)** may yield also **(9)** leading to **(6)** by decarboxylation. Alternatively, a non-degradative pathway may lead to **(10)** or **(11)** which, upon dehydrogenation, gives **(12)** [70]. Most of these intermediates have already been reported and are in agreement with previous reports in the literature [2,5].

3.6. *Stability and recyclability of mont-La (6%)-$Cu_{0.6}Cd_{0.4}S$*

Considering the importance of photocatalyst stability in practical applications, the recyclability of mont-La (6%)-$Cu_{0.6}Cd_{0.4}S$

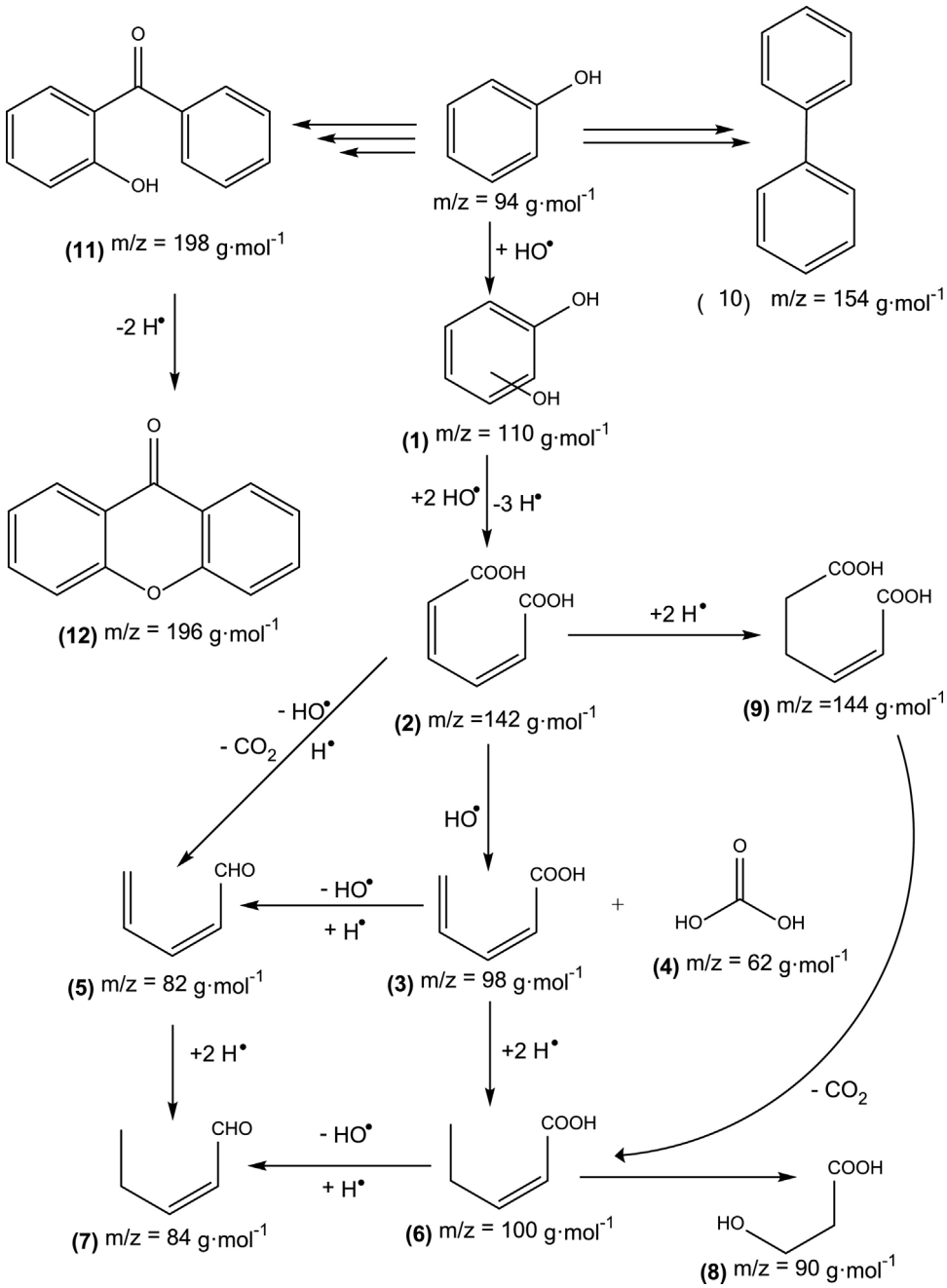

Fig. 12. Proposed reaction mechanism for the photocatalytic degradation of phenol. m/z ratios are rounded here, exact values are given in Table 1.

catalyst for phenol degradation was evaluated and the results are shown in Fig. 13.

In this work, phenol degradation experiments were repeated under near UV visible light irradiation using the optimized conditions for a sequence of 5 heterogeneous photocatalysis experiments using the same catalyst, which was washed with water and dried at 50 °C. Previous reports revealed that photoanodic corrosion in the photocatalytic reactions would lead to unstable metal sulfide semiconductors, and cause loss of stability of the photocatalyst during repeated experiments [59]. Hence, there were no significant changes in the photoactivity of the recycled catalyst after 5 cycles, confirming that mont-La (6%)-$Cu_{0.6}Cd_{0.4}S$ catalyst was a good photocatalytic material. 84% removal of phenol was obtained after five cycles. This excellent performance is attributed to a lowered recombination rate of the photogenerated e^-/h^+ and the effective suppression of the S^{2-} oxidization by the host layers of montmorillonite, which retarded the photocorrosion of the CdS and CuS.

Taking into account the composition of the catalyst, we have investigated by X-ray fluorescence the potential changes in its composition that might be due to photoinstability upon irradiation and may lead to undesirable leaching. Semiquantitative analysis of the catalyst, comparing the composition (expressed as % weight of oxides) before and after usage showed within experimental error, the same composition (ca. 4% CuO, 0.6% CdO and 0.2% La_2O_3). Therefore, no relevant leaching is expected upon irradiation, within the experimental conditions used.

Our result is in line to that obtained by Xiao et al. [62] in their study of the photocatalytic degradation of rhodamine B using CdS/rectorite nanocomposites.

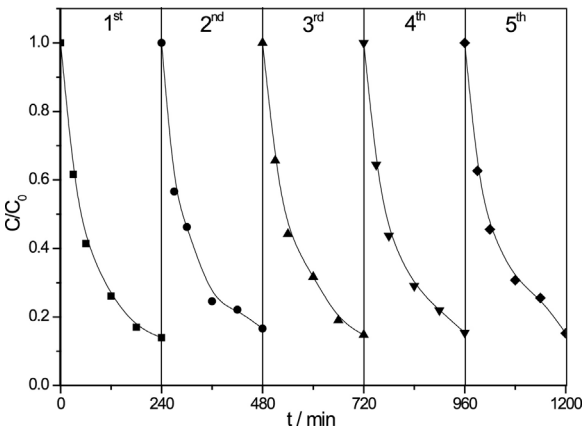

Fig. 13. Recycling performance of mont-La (6%)-$Cu_{0.6}Cd_{0.4}S$ catalyst toward phenol degradation under visible light irradiation.

4. Conclusion

This work explored the preparation of an effective and low-cost composite material by a simple impregnation approach using lanthanum chloride, copper acetate, cadmium and thiourea as precursors and montmorillonite clay as a support. The mont-La (6%)-$Cu_{0.6}$-$Cd_{0.4}$-S photocatalyst was used in near UV–vis (filter cut-off for $\lambda \leq 366$ nm) photodegradation of phenol in aqueous solution and presented high photocatalytic activity.

Photocatalyzed degradation of phenol in the presence of mont-La (6%)-$Cu_{0.6}Cd_{0.4}S$ follows pseudo-first order rate kinetics according to Langmuir–Hinshelwood model. The degradation rate was optimal with $1\,g\,L^{-1}$ initial catalyst loading and it decreases with increasing phenol concentration, likely due to the competition with HO^- for the same adsorption sites. It was found also that the Ar saturation decreases the photocatalytic activity for phenol removal, while it is not affected by increasing the natural dissolved oxygen concentration. Results also show that the degradation of phenol is more pronounced under acidic conditions. The effect of pH on the apparent pseudo-first order rate constants, increase in going from acidic to neutral conditions and decrease in alkaline media, suggesting that the optimal photocatalyzed degradation rate takes place when the surface is deprotonated and phenol molecules are in their neutral form. Under optimal conditions, phenol decomposition reached 86% and 77.8% TOC removal within 240 min. TOC removal rate was lower than the phenol decomposition rate, which is possibly caused by the generation of intermediates during phenol decomposition. This photocatalyst, mont-La (6%)-$Cu_{0.6}Cd_{0.4}S$, showed good stability after 5 cycles. Such high photocatalytic activity of the composite is due to the synergy effect of the montmorillonite support and the presence of copper sulfide associated with the photoactivity of cadmium sulfide co-catalyzed by lanthanium. This is, therefore, a promising photocatalyst for use with sunlight in green chemistry applications.

Acknowledgments

Horiya Boukhatem acknowledges the PNE program of the Algerian Ministry of Higher Education and Scientific Research for her pre-doctoral fellowship. This research was partially supported by the Group of Chemical Reactivity and Photoreactivity, University of A Coruña, with financial support from Ministerio de Economía y Competitividad (Spain) through project CTQ2015-71238-R (MINECO/FEDER). Partial support to this work came also from the Instituto de Catálisis y Petroleoquímica (CSIC) within the CTQ2013-48669-P project.

References

[1] S. Meshram, R. Limaye, S. Ghodke, S. Nigam, S. Sonawane, R. Chikate, Chem. Eng. J. 172 (2011) 1008–1015.
[2] H. Suzuki, S. Araki, H. Yamamoto, J. Water Process Eng. 7 (2015) 54–60.
[3] C. Valdés, J. Alzate-Morales, E. Osorio, J. Villaseñor, C. Navarro-Retamal, Chem. Phys. Lett. 640 (2015) 16–22.
[4] Y. Chen, J. He, Y.Q. Wang, T.A. Kotsopoulos, P. Kaparaju, R.J. Zeng, Biochem. Eng. J. 106 (2016) 19–25.
[5] E. Grabowska, J. Reszczyńska, A. Zaleska, Water Res. 46 (2012) 5453–5471.
[6] Z. Zeng, L. Tian, Z. Li, L. Jia, X. Zhang, M. Xia, Y. Hu, Biosens. Bioelectron. 69 (2015) 162–166.
[7] M. Kurian, R. Babu, J. Environ. Chem. Eng. 1 (2013) 86–91.
[8] F. Zhang, M. Li, W. Li, C. Feng, Y. Jin, X. Guo, J. Cui, Chem. Eng. J. 175 (2011) 349–355.
[9] Z. Wang, C. Wee Kee, S. Li, T.S. Andy Hor, J. Zhao, Appl. Catal. A: Gen. 393 (2011) 269–274.
[10] S. Suresh, V.C. Srivastava, I.M. Mishra, Chem. Eng. J. 171 (2011) 997–1003.
[11] A.A. Dougna, B. Gombert, T. Kodom, G. Djaneye-Boundjou, S.O.B. Boukari, N. Karpel Vel Leitner, L.M. Bawa, J. Photochem. Photobiol. A: Chem. 305 (2015) 67–77.
[12] I. Dobrosz-Gómez, M.Á. Gómez-García, S.M. López Zamora, E. GilPavas, J. Bojarska, M. Kozanecki, J.M. Rynkowski, C.R. Chim. 18 (2015) 1170–1182.
[13] H. Ling, K. Kim, Z. Liu, J. Shi, X. Zhu, J. Huang, Catal. Today 258 (2015) 96–102.
[14] R. Dhanalakshmi, M. Muneeswaran, K. Shalini, N.V. Giridharan, Mater. Lett. 165 (2016) 205–209.
[15] F. Wang, Y. Hu, C. Guo, W. Huang, C.Z. Liu, Bioresour. Technol. 110 (2012) 120–124.
[16] M. Canle L, M.I. Fernández, C. Martínez, J.A. Santaballa, Rev. Environ. Sci. Biotechnol. 11 (2012) 213–221.
[17] P. Wardman, J. Phys. Chem. Ref. Data 18 (4) (1989) 1637–1755.
[18] A. Turki, C. Guillard, F. Dappozze, Z. Ksibi, G. Berhault, H. Kochkar, Appl. Catal. B: Environ. 163 (2015) 404–414.
[19] Q. Zheng, H.J. Lee, J. Lee, W. Choi, N.B. Park, C. Lee, Chem. Eng. J. 249 (2014) 285–292.
[20] C.H. Chiou, C.Y. Wu, R.S. Juang, Sep. Purif. Technol. 62 (2008) 559–564.
[21] A. Shet, S.K. Vidhya, Solar Energy 127 (2016) 67–78.
[22] M. Fabiano de Almeida, C. Roberto Bellato, A. Honor Mounteer, S. Olavo Ferreira, J. Lopes Milagres, L.D. Lima Miranda, Appl. Surf. Sci. 357 (2015) 1765–1775.
[23] A.T. Nguyen, C.T. Hsieh, R.S. Juang, J. Taiwan Inst. Chem. Eng. 000 (2016) 1–8.
[24] J.J. Murcia, M.C. Hidalgo, J.A. Navío, J. Araña, J.M. Doña-Rodríguez, Appl. Catal. B: Environ. 179 (2015) 305–312.
[25] M.C. Hidalgo, J.J. Murcia, J.A. Navío, G. Colón, Appl. Catal. A: Gen. 397 (2011) 112–120.
[26] Z. Li, J. Sheng, Y. Zhang, X. Li, Y. Xu, Appl. Catal. B: Environ. 166–167 (2015) 313–319.
[27] J.Y. Hu, K. Tian, H. Jiang, Chemosphere 148 (2016) 34–40.
[28] F. Liang, Y. Zhu, Appl. Catal. B: Environ. 180 (2016) 324–329.
[29] Y. Wang, S. Indrawirawan, X. Duan, H. Sun, H.M. Ang, M.O. Tadé, S. Wang, Chem. Eng. J. 266 (2015) 12–20.
[30] M. Aslam, I.M.I. Ismail, N. Salah, S. Chandrasekaran, M. Tariq Qamar, A. Hameed, J. Hazard. Mater. 286 (2015) 127–135.
[31] A.M. Al-Hamdi, M. Sillanpää, J. Dutta, J. Alloys Compd. 618 (2015) 366–371.
[32] S. Kunduz, G.S. Pozan Soylu, Sep. Purif. Technol. 141 (2015) 221–228.
[33] Y.R. Jiang, W. William Lee, K.T. Chen, M.C. Wang, K.H. Chang, C.C. Chen, J. Taiwan Inst. Chem. Eng. 45 (2014) 207–218.
[34] Y. Wang, L. Zhou, X. Duan, H. Sun, E. Lee Tin, W. Jin, S. Wang, Catal. Today 258 (2015) 576–584.
[35] K. Hayat, M.A. Gondal, M.M. Khaled, S. Ahmed, A.M. Shemsi, Appl. Catal. A: Gen. 393 (2011) 122–129.
[36] I. Fatimah, J. Adv. Res. 5 (2014) 663–670.
[37] E.G. Garrido-Ramírez, J.F. Marco, N. Escalona, M.S. Ureta-Zañartu, Microporous Mesoporous Mater. 225 (2016) 303–311.
[38] H. Rezala, H. Khalaf, J.L. Valverde, A. Romero, A. Molinari, A. Maldotti, Appl. Catal. A: Gen. 352 (2009) 234–242.
[39] H. Rezala, J.L. Valverde, A. Romero, A. Molinari, A. Maldotti, Mor. J. Chem. 3 (2) (2015) 314–330.
[40] S. Ouidri, H. Khalaf, J. Photochem. Photobiol. A: Chem. 207 (2009) 268–273.
[41] B. Damardji, H. Khalaf, L. Duclaux, B. David, Appl. Clay Sci. 44 (3–4) (2009) 201–205.
[42] P. Pichat, H. Khalaf, D. Tabet, M. Houari, M. Saidi, Environ. Chem. Lett. 2 (2005) 191–194.
[43] D. Tabet, D. Robert, P. Pichat, H. Khalaf, Desalin. Water Treat. 13 (2010) 437–440.
[44] N. Khaorapapong, M. Ogawa, Appl. Clay Sci. 35 (2007) 31–38.
[45] N. Khaorapapong, M. Ogawa, Phys. Chem. Solids 69 (2008) 941–948.
[46] N. Khaorapapong, K. Kuroda, H. Hashizume, M. Ogawa, Appl. Clay Sci. 19 (2001) 69–76.
[47] N. Khaorapapong, A. Ontam, M. Ogawa, Mater. Lett. 62 (2008) 3722–3723.
[48] N. Khaorapapong, A. Ontam, S. Youngme, M. Ogawa, Phys. Chem. Solids 69 (2008) 1107–1111.
[49] N. Khaorapapong, A. Ontam, J. Khemprasit, M. Ogawa, Appl. Clay Sci. 43 (2009) 238–242.

[50] M.F. Brigatti, E. Galan, B.K.G. Theng, in: F. Bergaya, G.K.B. Theng, G. Lagaly (Eds.), Handbook of Clay Science, vol. 1, Elsevier, Amsterdam, 2006, pp. 19–86.
[51] R.J. Sengwa, S. Choudhary, S. Sankhla, Colloids Surf. A: Physicochem. Eng. Aspects 336 (2009) 79–87.
[52] M. Saranya, R. Ramachandran, E.J. Jebaseelan Samuel, S.K. Jeong, A.N. Grace, Powder Technol. 279 (2015) 209–220.
[53] H. Ren, W. Xu, S. Zhua, Z. Cui, X. Yang, A. Inoue, Electrochim. Acta 190 (2016) 221–228.
[54] M. Saranya, C. Santhosh, R. Ramachandran, P. Kollu, P. Saravanan, M. Vinoba, S.K. Jeong, A.N. Grace, Powder Technol. 252 (2014) 25–32.
[55] Y. Im, B.S. Kwak, M. Kang, Powder Technol. 267 (2014) 103–110.
[56] J. Ru, Z. Huayue, L. Xiaodong, X. Ling, Chem. Eng. J. 152 (2009) 537–542.
[57] H. Boukhatem, L. Djouadi, N. Abdelaziz, H. Khalaf, Appl. Clay Sci. 72 (2013) 44–48.
[58] D.V. Markovskaya, S.V. Cherepanova, A.A. Saraev, E.Y. Gerasimov, E.A. Kozlova, Chem. Eng. J. 262 (2015) 146–155.
[59] Q. Wang, Y. Shi, L. Pu, Y. Ta, J. He, S. Zhang, J. Zhong, J. Li, B. Su, Appl. Surf. Sci. 367 (2016) 109–117.
[60] C. Martínez, M. Canle L, M.I. Fernández, J.A. Santaballa, J. Faria, Appl. Catal. B: Environ. 107 (2011) 110–118.
[61] D. Chen, Y. Du, H. Zhu, Y. Deng, Appl. Clay Sci. 87 (2014) 285–291.
[62] J. Xiao, T. Peng, K. Dai, L. Zan, Z. Peng, J. Solid State Chem. 180 (2007) 3188–3195.
[63] G. Yang, B. Yang, T. Xiao, Z. Yan, Appl. Surf. Sci. 283 (2013) 402–410.
[64] Y. Bessekhouad, M. Mohammedi, M. Trari, Solar Energy Mater. Solar Cells 73 (2002) 339–350.
[65] B.T. Raut, M.A. Chougule, S. Sen, R.C. Pawar, C.S. Lee, V.B. Patil, Ceram. Int. 38 (2012) 3999–4007.
[66] A. Nezamzadeh-Ejhieh, H. Zabihi-Mobarakeh, J. Ind. Eng. Chem. 20 (2014) 1421–1431.
[67] T. Jiang, W. Liu, Y. Mao, L. Zhang, J. Cheng, M. Gong, H. Zhao, L. Dai, S. Zhang, Q. Zhao, Chem. Eng. J. 259 (2015) 603–610.
[68] J. Qian, K. Wang, Q. Guan, H. Li, H. Xu, Q. Liu, W. Liu, B. Qiu, Appl. Surf. Sci. 288 (2014) 633–640.
[69] L.J. Zhang, T.F. Xie, D.J. Wang, S. Li, L.L. Wang, L.P. Chen, Y.C. Lu, Int. J. Hydrogen Energy 38 (2013) 11811–11817.
[70] H. Chun, W. Yizhong, T. Hongxiao, Chemosphere 41 (2000) 1205–1209.
[71] S.G. Poulopoulos, F. Arvanitakis, C.J. Philippopoulos, J. Hazard. Mater. B 129 (2006) 64–68.
[72] T.T.T. Dang, S.T.T. Le, D. Channei, W. Khanitchaidecha, A. Nakaruk, Res. Chem. Intermed. 42 (2016) 5961–5974.
[73] K. Naeem, O. Feng, J. Environ. Sci. 21 (2009) 527–533.
[74] T.Y. Wei, C.C. Wan, Ind. Eng. Chem. Res. 30 (1991) 1293–1300.
[75] C. Martínez, M. Canle L, M.I. Fernández, J.A. Santaballa, J. Faria, Appl. Catal. B: Environ. 102 (2011) 563–571.
[76] S. Ahmed, M.G. Rasul, W.N. Martens, R. Brown, M.A. Hashib, Desalination 261 (2010) 3–18.
[77] K.M. Parida, S. Parija, Solar Energy 80 (2006) 1048–1054.
[78] H. Khizar, M.A. Gondal, M.K. Mazen, A. Shakeel, J. Mol. Catal. A: Chem. 336 (2011) 64–71.
[79] J. Miao, Z. Jia, H.B. Lu, D. Habibi, L.C. Zhang, J. Taiwan Inst. Chem. Eng. 45 (2014) 1636–1641.
[80] M. Canle L, J.A. Santaballa, E. Vulliet, J. Photochem. Photobiol. A: Chem. 175 (2005) 192.
[81] R.R. Solís, F.J. Rivas, J.L. Pérez-Bote, O. Gimeno, J. Taiwan Inst. Chem. Eng. 46 (2015) 125–131.
[82] Albert, E.P. Serjeant, Ionization Constants of Acids and Bases. A Laboratory Manual, Methuen & Co., London, 1962.
[83] E. Pecini, M. Avena, Langmuir 29 (2013) 14926–14934.
[84] Y. Wu, H. Luo, H. Wang, L. Zhang, P. Liu, L. Feng, J. Colloid Interface Sci. 436 (2014) 90–98.